ARTICLE

CNT-based bifacial perovskite solar cells toward highly efficient 4-terminal tandem photovoltaics

Chunyang Zhang,[a,b] Min Chen,[c] Fan Fu[d], Hongwei Zhu[b], Thomas Feurer[d], Wenming Tian,[e] Chao Zhu,[f] Ke Zhou,[g] Shengye Jin,[e] Shaik Mohammed Zakeeruddin,[b] Ayodhya N. Tiwari,[d] Nitin P. Padture,[c] Michael Grätzel[b,*] and Yantao Shi[a,*]

Carbon-based perovskite solar cells (C-PSCs) are recognized as low-cost stable photovoltaics. However, currently most highly efficient C-PSCs are optically opaque, which means that they can only utilize direct illumination but cannot efficiently utilize the reflected irradiance. Here we propose bifacial C-PSCs incorporating transparent carbon-nanotube (CNT) network films in the rear electrode to efficiently utilize the reflected irradiation. The CNT-PSCs show monofacial-power-conversion-efficiency (monofacial-PCE) up to 21.4%, whereas the CNT-PSCs reach bifacial power output of 24.0 mW cm^2 in natural reflecting surroundings (20% of AM 1.5G irradiance) and 34.1 mW cm^2 in artificial reflecting surroundings (100% of AM 1.5G irradiance). The bifacial CNT-PSCs also show high operational stability with a loss 5% under 1000 h full sun continuous illumination. Moreover, we achieved a PCE of 27.1% by using our bifacial device as a top cell together with a CIS bottom cell in a 4-T tandem. These findings point to a promising direction for improving the output power per unit area of PSCs.

Broader context

For solar cells, how to increase the power output per active area is an eternal pursue. However, currently almost all types of solar cells are optically opaque (namely monofacial solar cells), which means that they can only utilize direct illumination but cannot utilize the reflected irradiance (albedo) that is pervasive in real-world conditions. Furthermore, these monofacial solar cells are not applicable to fabricate four-terminal (4-T) tandem solar cells. Developing advanced bifacial photovoltaics has long been a goal to pursue high output per unit active area and to fabricate highly efficient 4-T solar cells. The key to obtain efficient bifacial photovoltaics is to develop highly conductive transparent electrode and to prepare high efficiency semi-transparent solar cells, which is of great importance but very challenging.

Introduction

Semiconducting perovskite materials have drawn tremendous attention in the past decade due to their excellent photovoltaic (PV) properties such as a large light absorption coefficient, long carrier diffusion length, and robust defect tolerance.[1-7] Monofacial perovskite solar cells (PSCs) have

[a] State Key Laboratory of Fine Chemicals, School of Chemistry, Dalian University of Technology, Dalian, 116024, China. Email: shiyantao@dlut.edu.cn
[b] Laboratory of Photonics and Interfaces (LPI), Department of Chemistry and Chemical Engineering, École Polytechnique Fédérale de Lausanne (EPFL), CH-1015 Lausanne, Switzerland. Email: michael.graetzel@epfl.ch
[c] School of Engineering, Brown University, Providence, Rhode Island 02912, United States.
[d] Laboratory for Thin Films and Photovoltaics, Empa-Swiss Federal Laboratories for Materials Science and Technology, CH-8600 Duebendorf, Switzerland.
[e] State Key Laboratory of Molecular Reaction Dynamics, Dalian Institute of Chemical Physics, Chinese Academy of Sciences, Dalian, 116023, China.
[f] SEU-FEI Nano-Pico Center, Key Laboratory of MEMS of Ministry of Education, Collaborative Innovation Center for Micro/Nano Fabrication, Device and System, Southeast University, Nanjing 210096, P. R. China
[g] Department of Chemistry & College of Chemistry and Chemical Engineering, Xiamen University, Xiamen 361005, China.
C. Y. Zhang, M. Chen and Fan Fu contributed equally.
Electronic Supplementary Information (ESI) available: [details of any supplementary information available should be included here]. See DOI: 10.1039/x0xx00000x

reached a certified power conversion efficiency (PCE) of 25.5% based on direct AM 1.5G irradiation, which is comparable to the efficiency of Si-based solar cells.[1, 8] The rapid development of the PSCs, and their impact on the global renewable energy landscape is driving a huge amount of effort worldwide in commercializing PSCs technology.[9, 10] However, the PCE of monofacial PSCs panel relies mainly on ideal AM 1.5G irradiance, and such direct irradiation is reduced due to azimuth and tilt angles in real-world conditions.[11-15] Moreover, the additional reflected irradiation is typically more than 20% of AM 1.5G irradiance in natural reflecting surroundings and could increase to 100% of AM 1.5G irradiance by introducing artificial reflecting surroundings, which is wasted in the prevailing monofacial PSCs.[12, 16-25] Thus, there is an urgent need to develop PSCs to take advantage of the albedo by efficiently utilizing the reflected irradiation.[26, 27] As a result, the bifacial PSCs panels have been proposed to convert both direct and reflected irradiation to electricity, and increase the output power of modules with minimal additional cost.[12, 28]

The main challenge for preparing high-performance bifacial PSCs lies in replacing the opaque metal rear electrode with a

transparent and conductive charge collector using a simple and economical fabrication method. This would allow the transmission of the reflected light through the rear electrode to guarantee high bifacial light absorption.[11, 24] Recently, various strategies have been implemented to develop transparent and conductive rear electrodes.[29, 30] Significant amount of research has been devoted to developing an ultra-thin metal electrode that include, but are not limited to, silver (Ag), gold (Au), aluminum (Al), and copper (Cu). However, these ultra-thin metal electrodes suffered from visible light absorption due to their plasmonic effect, and relatively low stability in air.[16, 31] In order to replace the metal electrode, transparent conductive oxides (TCOs), carbon-based materials and organic conductive polymers have been used.[32-34] Fu, *et. al*. reported a sputtered hydrogenated indium oxide (In_2O_3:H) as transparent rear electrode, and realized a 14.5%-PCE hysteresis-free planar PSC[35]. Peng, *et. al*. reported the use of chemical vapor deposited (CVD) graphene as transparent rear electrode, and realized a 12.4%-PCE semitransparent PSC.[32] Park, *et. al.* reported the PEDOT:PSS as transparent rear electrode, and realized a 13.6%-PCE semitransparent PSC.[36] Obviously, the PCEs of nonmetallic electrode devices are greatly reduced. This will inevitably lead to the lower bifacial power output, which maybe even lower than monofacial power output of the mainstream device and defeats the purpose of designing bifacial devices.

The key to increase the PCEs of nonmetallic electrode devices is to improve the charge collection ability of the back electrode. To solve this problem, in our previous work, we designed a new type of stable and efficient modular carbon-based PSC.[33] The PCE of the modular graphene-based PSC is greatly improved to 18.6% by combining conductive substrate (i.e., FTO, Al foil et. al) and carbon electrode. However, the poor bifaciality of the graphene-based PSC (~30%, ratio of PCE when illuminated from the front- and rear-sides) have a limited ability to increase the bifacial output power. Therefore, the key to greatly improve the bifacial output power of the modular carbon-based PSCs is to achieve both the efficient monofiicial-PCE and high bifaciality.

Herein we report a transparent electrode incorporating carbon-nanotube (CNT) network on fluorinated tin oxide (FTO) TCO as a new type of transparent electrode, which demonstrates good extraction and transport of photo-induced holes due to its high electrical conductivity. By optimizing the type and size of the CNTs, we enhance the monofacial-PCE of the bifacial PSCs to 21.4% subjected to only direct irradiation. This corresponds to the highest PCE reported so far for a bifacial PSCs prepared at low temperatures (<85 °C). The bifacial power output under the standard test (IEC TS 60904-1-2) is 24.0 mWcm^{-2} for naturally reflecting surroundings (20% of AM 1.5G irradiance) and 34.1 mWcm^{-2} for the artificially reflecting surroundings (100% of AM 1.5G irradiance). We further show that the bifacial PSCs are operationally stable under one-sun illumination for over 1000 h. More importantly, when coupling our bifacial solar cell with a 1.0-eV $CuInSe_2$ (CIS) solar cell, we achieve 27.1%-efficient perovskite/CIS thin film tandem solar cells.

Results and discussion

To examine the extraction ability of photo-induced holes of the CNT-based transparent electrode, we employ the layered architecture glass/perovskite/spiro-OMeTAD/CNT, (Fig. 1a). The representative multiwall carbon nanotube (MWCNT/1) material is dispersed into isopropanol solution after ball-milling for 12 h and sprayed on the HTL. The optical image of the MWCNT/1 network (Fig. 1d) shows the radius of the prepared MWCNT/1 to be about 40~100 nm. The radius of the MWCNT/1 is further confirmed by the transmission electron microscope (TEM) picture shown in Fig. S1. We sprayed a specific (double-circle-like) shape of MWCNT/1 network on the HTL layer for the following model experiments. As illustrated in Fig. 1b and 1c, the photo-induced holes will be transported through the HTL and collected by MWCNT/1 network. Thus, severe photoluminescence (PL) quenching effect will be further strengthened at the interface between MWCNT/1 network and HTL position. When exposed to a short pulse light excitation, the PL quenching effect could be clearly monitored in the widened particular shape of the MWCNT/1 network (Fig. 1e). The enlarged PL quenching region compared with the primitive shape of MWCNT/1 network could be explained by the wide active region by Ohmic contact between MWCNT/1 network and HTL. Fig. 1f shows the scanning electron microscope (SEM) image for the prepared MWCNT/1 network electrode used in the bifacial PSCs. The decent coverage of MWCNT/1 network with the wide active region guarantees effective holes-collection from the HTL by the MWCNT/1 network

To utilize the transparent CNT network electrode in the device level, a semi-cell A was fabricated by sequentially depositing SnO_2 electron-transport layer (ETL), perovskite layer, spiro-OMeTAD hole-transport layer (HTL), and MWCNT/1 network, while another charge collector B was prepared by spraying the MWCNT/1 network on the FTO/glass substrate. The final cell illustrated in Fig. 2a was thus achieved by stacking the semi-cell A and charge collector B under a small pressure (0.0025 MPa). The thickness (8.7 μm) of MWCNT/1 film obtained from depositing 500 μL of MWCNT/1 slurry (4 mg/ml isopropanol solution) was determined by the cross-sectional SEM image of the MWCNT/1 film as shown in Fig. S2. Based on the linear relationship between the CNT layr thickness and the deposited volume of the MWCNT/1 slurry, we varied the thickness simply by changing the volume of dispersion slurry of MWCNT/1. Fig. 2b shows that the monofacial-PCE obtained from the prepared cells is sharply increasing with the thickness of the MWCNT/1 films due to the lower sheet resistance. More details of the photovoltaic parameters are summarized in Table S1 and S2. The gradual decrease of PCE in thicker MWCNT/1 films may be rationalized by the elongation of the transportation path for the photo-induced holes and lowering

of the shunt resistance at the device level, leading to the lower open circuit coltage (V_{oc}) and fill factor (FF). Thus, the champion PCE obtained from the *J-V* curves (Fig. S3) in the semi cell is 14.4% with the 4.0 μm MWCNT/1 film thickness. The monofacial-PCE value (Fig. S4) is further improved to 18.7% in the final cell with the 0.4 μm MWCNT/1 film thickness. The higher monofacial-PCE with decreasing MWCNT/1 film thickness is due to a substantial contribution in the electrical conductivity from the incorporation of FTO in the hole collector electrode. The morphology of the 400 nm thick MWCNT/1 film is recorded in Fig. S5. A clear MWCNT/1 network is presented with uniform spatial distributions of the multijunction between the adjacent carbon nanotubes. We also subjected the monofacial-PCE to illumination from the rear side yielding a very low PCE value of 0.6 % calculated from the *J-V* curves in Fig. 2c compared to a PCE of 18.7% for the front illumination. The inset-Fig. 2c shows the steady-state power output (SPO_{bi}) of the prepared solar cells, which is consistent with the monofaicial-PCE. Fig. 2d shows that the poor transmittance for light across the visible light region by the 400 nm thick MWCNT/1 film is responsible for the poor performance. The external quantum efficiency (EQE) and intergrated current density of MWCNT/1-based bifacial solar cell illuminated from front side and rear side are illustrated in the Fig. 2e, matching with the J_{SC} value. The specific photovoltaic metrics of the MWCNT/1-based PSCs illuminated separately from the front and rear side are summarized in Table S3.

To enhance the transmittance of the sprayed carbon nanotube films, we further change the multiwall carbon nanotubes to diameter of 10 nm (MWCNT/2) as illustrated in Fig. 3a and 3b. The as-sprayed thin film also demonstrates a dense network morphology as shown in Fig. S6a. Moreover, the single-wall carbon nanotubes with radius of 2 nm (SWCNT) is also utilized here to enhance the transmittance (Fig. 3d, 3e and S6b). Both MWCNT/2 and SWCNT shows superior electrical conductivity (Fig. S7) compared with the MWCNT/1 in the linear sweep voltammetry (LSV) experiment illustrated in Fig. S8. However, the optical transmittance (Fig. S9) from SWCNT is higher across the visible light region than that of the MWCNT/2 films at the same thickness, which explains the better bifacial PV performance realized by the SWCNT-PSC. In Fig. 3c and 3f, the monofacial-PCE from MWCNT/2-PSCs is 22.2% for front illumination and 10.8% for rear illumination while the respective values for the monofacial-PCE obtained with SWCNT-PSCs are 21.4% and 16.8%. These PCE values are also consistent with the EQE results and integrated current densities in Fig. S10. The PV performance parameter statistics of bifacial CNT-PSC illuminated from front side based on MWCNT/2 and SWCNT electrode is summarized in Fig. 3g and the steady-state PCE of MWCNT/2-PSC and SWCNT-PSC is shown in Fig. S11. Details of the photovoltaic metrics are summarized in Table 1. It should be noted that, while the monofacial-PCE from MWCNT/2-PSCs from front illumination is slightly higher than the monofacial-PCE from SWCNT-PSCs, the monofacial-PCE from SWCNT-PSCs

from rear illumination is significantly higher than the monofacial-PCE from MWCNT/2-PSCs. Typical unencapsulated MWCNT/2-PSC and SWCNT-PSC were chosen for stability testing in N_2 atmosphere (25 °C) under continuous one sun illumination. The continuous maximum power point tracking of the PV performance (Fig. 3h and S12) shows that the devices maintained 95% of their initial PCE after 1000 h continuous operation for both MWCNT/2-PSC and SWCNT-PSC. This clearly demonstrates the high operational stability for MWCNT/2-PSC and SWCNT-PSC, which is consistent with the excellent coverage of the CNT network films that reduces the exposure of the PSCs to ambient moisture and oxygen.

Both MWCNT/2-PSC and SWCNT-PSC exhibit a great potential in the bifacial solar cell application. Thus, the theoretical modeling is performed to predict the bifacial-PV performance of MWCNT/2-PSC and SWCNT-PSC. Fig. 4a and 4b presents a schematic diagram of bifacial solar cell used in the natural and artificial reflected surroundings. In the natural reflected surroundings, the cloud and the ground will offer additional diffuse reflected irradiance from the sunlight illumination. The total reflected irradiance to the rear side of bifacial solar cells could be approximately 20% of the AM 1.5G to the front side of bifacial solar cells. However, in the artificial reflected surroundings, a simple mirror structure could be designed here to perform the specular reflection of AM 1.5G to the rear side of bifacial solar cells. In this circumstance, 100% or more of the AM 1.5G could be achieved. According to the following formulas, the simulation of the PV performance ($V_{oc\text{-}bi}$, $I_{sc\text{-}bi}$, FF_{bi}, and PO_{bi}) based on the front side electrical parameter ($V_{oc\text{-}f}$, $I_{sc\text{-}f}$, FF_f and η_f)rear side short circuit current ($I_{sc\text{-}f}$) under standard test conditions and the rear side irradiance (x) is performed.[15, 37, 38] Due to series resistance in PSCs, open-circuit voltage of the bifacial solar cells ($V_{oc\text{-}bi}$, Fig. S13a) is gradually increasing and its fill factor (FF_{bi}, Fig. S13c, Equation 3) is decreasing with the enhancement of rear side irradiance (x) based on Equation 1. The short-circuit current of the bifacial solar cells ($J_{sc\text{-}bi}$, Fig. S13b) is dramatically increasing with the higher rear side irradiance (x) based on the Equation 2. This could be attributed to the high photocurrent density proportional to the additional absorbed photon flux in the bifacial solar cells. In all, the theoretical equivalent bifacial power output (PO_{bi}, Equation 4) is summarized in the Fig. 4c and the SWCNT-PSCs shows the highest theoretical PV performance in the bifacial solar cells under higher rear-side irradiance region. It should be noted that the predicted bifacial power output per unit area (34.4 mW cm^{-2}) of MWCNT/2-PSCs in the artificial reflected surroundings has the potential to be equivalent to the monofacial power output per unit area from monofacial-PSCs up to 34.4%.

$$V_{oc-bi} = V_{oc-f} \frac{\ln\left(R_{Isc}\frac{I_{sc-f}}{I_0}\right)}{\ln\left(\frac{I_{sc-f}}{I_0}\right)} = V_{oc-f} + 0.026\ln(1+\frac{I_{sc-r}}{I_{sc-f}}x) \qquad \textit{Equation 1}$$

$$I_{sc-bi} = R_{Isc}I_{sc-f} = I_{sc-f} + (I_{sc-r})x \qquad \textit{Equation 2}$$

$$FF_{bi} = FF_f\left[R_{lsc} - (R_{lsc} - 1)\frac{pFF}{FF_f}\right] = FF_f + \frac{I_{sc-r}}{I_{sc-f}}\left[FF_f - \frac{\frac{V_{oc-f}}{0.026} - \ln(\frac{V_{oc-f}}{0.026} - 0.72)}{\frac{V_{oc-f}}{0.026} + 1}\right]x \quad \textit{Equation 3}$$

$$PO_{bi} = \eta_f R_{lsc}\left[R_{lsc} - (R_{lsc} - 1)\frac{pFF}{FF_f}\right]\frac{\ln\left(R_{lsc}\frac{I_{sc-f}}{I_0}\right)}{\ln\left(\frac{I_{sc-f}}{I_0}\right)} \quad \textit{Equation 4}$$

We measured the bifacial-PV performance of MWCNT/2-PSCs by the PSC devices of the architecture shown in Fig. 2a. The cross-section of the semi-cell A in SWCNT-PSCs is presented in Fig. 4d. Due to the limitation of the experimental setup, single light source method is used here to examine the bifacial power output of SWCNT-PSC. One equivalent indoor characterization standard method described in IEC TS 60904-1-2 are introduced as single light source method (Fig. S14) in the measurement for the bifacial PV performance.[21, 24, 38] For single light source method, an equivalent irradiance (total of standard test condition irradiance and rear-side irradiance G_{rear} multiplied by bifacially factor φ=min (I_{rear}/I_{front}, P_{rear}/P_{front})) is projected onto the front-side of the test module. The 20% and 100% of AM 1.5G irradiance were chosen to represent the natural reflected surroundings and artificial reflected surroundings, respectively. In the natural reflected surroundings, the PO_{bi} from J-V curves is 24.6 mW cm^{-2} (Fig. 4e). Under the artificial albedo condition, the reverse scan of the J-V curves shows a V_{oc} of 1.136 V, a J_{sc} of 43.6 mA.cm^{-2}, an FF of 0.694 and a PO_{bi} of 34.3 mW cm^{-2}. Detailed performance parameters are summarized in Table S4. To further confirm the bifacial-PV performance, we also utilized the double light source method described in IEC TS 60904-1-2 to test the PCE values. Such standard test is illustrated in Fig. S15a, where the tested solar cells is under continuous AM.1.5G illumination calibrated by a Si reference cell from the front and rear side simultaneously enabled by the mirror design.[24, 25] Under the standard test method, the SPO_{bi} obtained (Fig. S15b and S16 and Table S5) is still 34.2 W m^{-2}. The solid bifacial-PV performance clearly demonstrates the potential of bifacial PSCs to boost the equivalent bifacial-PCE performance by utilizing the additional reflected irradiance. The SWCNT-PSCs are further developed to construct perovskite/CIS tandem solar cells in 4-terminal (4-T) configuration where the SWCNT-PSC is acting as the top cell (Fig. 5a). A state-of-the-art CIS with 1.0 eV band gap is used as the bottom cell. The J-V curves of the 4-T tandem devices are shown in Fig. 5b. The standalone CIS solar cell exhibits a PCE of 17.9% with the V_{oc} of 0.584 V, the J_{sc} of 42.0 mA.cm^{-2} and the FF of 0.731. The filtered CIS cell yields of a PCE of 5.7% with a V_{oc} of 0.549 V, a J_{sc} of 14.3 mA.cm^{-2} and an FF of 0.724. All of the J_{sc} values are consistent with the intergraded values from EQE spectra shown in Fig. 5c. When paired with the 21.4% SWCNT-PSC top cell, the PCE of SWCNT-PSC/CIS tandem solar cell reaches 27.1% in 4-T tandem configuration. The specific PV parameters for SWCNT-PSC/CIS 4-terminal tandem solar cell are summarized in Table 2.

Conclusions

We have shown that the CNT network films sprayed at low temperature show are capable of extracting the photo-induced holes from the HTL there dense structure assuring a good coverage of the HTL. PSCs based on the CNT network films exhibit a PCE of 21.4 % when illuminated only from the front side. The monofacial-PV performance was further improved by changing the type and radius of the CNT hole collector. Bifacial illumination in natural albedo (20% of AM 1.5G irradiance) produce a power output of 24.0 W m^{-2} increasing to 34.1 W m^{-2} in artificial reflecting surroundings (100% of AM 1.5G irradiance). The sprayed CNT network films also protected PSCs from the environmental stress. The PCE degraded to only 95% of the initial PCE after 1000 h continuous operation. More importantly, when coupling our bifacial solar cell with a 1.04-eV CIS solar cell, we achieve 27.1%-efficient perovskite/CIS thin film tandem solar cells. Based on all our results, we envision the bifacial PSCs incorporating the CNT-network films pointing to a fruitful research direction for developing stable PSCs accommodated in the complicated irradiation condition and efficiently utilizing the reflected irradiation. These results also have implications on the development of the prevailing perovskite-based tandem photovoltaics.

Author Contributions

Y. T. S and C. Y. Z conceived the idea and designed the research route, C. Y. Z conducted the overall experimental investigations. M. C. and C. Y. Z contributed to data analysis and manuscript origanization. M. G supervised the project and contributed to manuscript modification. F. F. performed the 4-terminal tandem measurement. T. F. fabricated the CIS solar cells. K. Z and M.C. offered important suggestions and contributed greatly in both the experiment design and manuscript arrangement. Y. T. S, A. N. T, N. P. P, S. M. Z modified the manuscript and were involved in the discussion and provided support in project coordination. C. Z conducted HTEM characterizations. S. Y. J and W. M. T conducted PL mapping characterizations. All the authors contributed toward finalizing the manuscript.

Conflicts of interest

There are no conflicts to declare.

Acknowledgements

Notes and references

1.　Y. Liu, S. Akin, L. Pan, R. Uchida, N. Arora, J. V. Milić, A. Hinderhofer, F. Schreiber, A. R. Uhl and S. M. Zakeeruddin, *Sci. Adv.*, 2019, **5**, eaaw2543.

2.　Y.-H. Lin, N. Sakai, P. Da, J. Wu, H. C. Sansom, A. J. Ramadan, S. Mahesh, J. Liu, R. D. Oliver and J. Lim, *Science*, 2020, **369**, 96.

3.　X. Tian, S. D. Stranks and F. You, *Sci. Adv.*, 2020, **6**, eabb0055.

4.　S. Yang, S. Chen, E. Mosconi, Y. Fang, X. Xiao, C. Wang, Y. Zhou, Z. Yu, J. Zhao and Y. Gao, *Science*, 2019, **365**, 473.

5.　B. Chen, S.-W. Baek, Y. Hou, E. Aydin, M. De Bastiani, B. Scheffel, A. Proppe, Z. Huang, M. Wei and Y.-K. Wang, *Nat. Commun.*, 2020, **11**, 1.

6.　R. Lin, K. Xiao, Z. Qin, Q. Han, C. Zhang, M. Wei, M. I. Saidaminov, Y. Gao, J. Xu and M. Xiao, *Nat. Energy*, 2019, **4**, 864.

7.　Z. Yang, Z. Yu, H. Wei, X. Xiao, Z. Ni, B. Chen, Y. Deng, S. N. Habisreutinger, X. Chen and K. Wang, *Nat. Commun.*, 2019, **10**, 1.

8.　M. A. Green, E. D. Dunlop, J. Hohl‐Ebinger, M. Yoshita, N. Kopidakis and X. Hao, *Progress in Photovoltaics: Research and Applications*, 2020, **28**, 629.

9.　T. Leijtens, K. A. Bush, R. Prasanna and M. D. McGehee, *Nat. Energy*, 2018, **3**, 828.

10.　W. Li, J. Zheng, B. Hu, H.-C. Fu, M. Hu, A. Veyssal, Y. Zhao, J.-H. He, T. L. Liu and A. Ho-Baillie, *Nature Materials*, 2020, 1.

11.　R. Kopecek and J. Libal, *Nat. Energy*, 2018, **3**, 443.

12.　J. Wu, Y. Li, Q. Tang, G. Yue, J. Lin, M. Huang and L. Meng, *Sci. Rep.*, 2014, **4**, 1.

13.　S. H. Moon, S. J. Park, Y. J. Hwang, D.-K. Lee, Y. Cho, D.-W. Kim and B. K. Min, *Sci. Rep.*, 2014, **4**, 1.

14.　J. Duan and Q. Tang, *Dalton Trans.*, 2019, **48**, 799.

15.　J. F. Martínez, M. Steiner, M. Wiesenfarth, T. Fellmeth, T. Dörsam, M. Wiese, S. W. Glunz and F. Dimroth, *Progress in Photovoltaics: Research and Applications*, 2020, **28**, 349.

16.　L. Fan, Y. Li, X. Yao, Y. Ding, S. Zhao, B. Shi, C. Wei, D. Zhang, B. Li and G. Wang, *ACS Applied Energy Materials*, 2018, **1**, 1575.

17.　R. Hezel, *Progress in Photovoltaics: Research and Applications*, 2003, **11**, 549.

18.　A. Cuevas, A. Luque, J. Eguren and J. del Alamo, *Solar Energy*, 1982, **29**, 419.

19.　R. Guerrero Lemus, R. Vega, T. Kim, A. Kimm and L. Shephard, *Renewable and Sustainable Energy Reviews*, 2016, **60**, 1533.

20.　J. Bisquert, *Nat. Photonics*, 2008, **2**, 648.

21.　T. S. Liang, M. Pravettoni, C. Deline, J. S. Stein, R. Kopecek, J. P. Singh, W. Luo, Y. Wang, A. G. Aberle and Y. S. Khoo, *Energy Environ. Sci.*, 2019, **12**, 116.

22.　S. Pal and R. Saive, 2019.

23.　D. Marongiu, S. Lai, V. Sarritzu, E. Pinna, G. Mula, M. L. Mercuri, M. Saba, F. Quochi, A. Mura and G. Bongiovanni, *ACS Appl. Mater. Interfaces*, 2019, **11**, 10021.

24.　M. G. Borrull, *Performance optimization of bifacial module PV power plants based on simulations and measurements*, 2019.

25.　C. Monokroussos, Q. Gao, X. Zhang, E. Lee, Y. Wang, C. Zou, L. Rimmelspacher, J. B. Castro, M. Schweiger and W. Herrmann, *Progress in Photovoltaics: Research and Applications*, 2020.

26.　S. Ito, S. M. Zakeeruddin, P. Comte, P. Liska, D. Kuang and M. Grätzel, *Nat. Photonics*, 2008, **2**, 693.

27.　H. Wang, H. A. Dewi, T. M. Koh, A. Bruno, S. Mhaisalkar and N. Mathews, *ACS Appl. Mater. Interfaces*, 2019, **12**, 484.

28.　P. Tillmann, K. Jäger and C. Becker, *Sustainable Energy & Fuels*, 2020, **4**, 254.

29.　Y. Duan, Q. Tang, J. Liu, B. He and L. Yu, *Angew. Chem. Int. Ed.*, 2014, **53**, 14569.

30.　Q. Tai, B. Chen, F. Guo, S. Xu, H. Hu, B. Sebo and X.-Z. Zhao, *ACS Nano*, 2011, **5**, 3795.

31.　D. Chen, S. Pang, L. Zhou, X. Li, A. Su, W. Zhu, J. Chang, J. Zhang, C. Zhang and Y. Hao, *J. Mater. Chem. A*, 2019, **7**, 15156.

32.　P. You, Z. Liu, Q. Tai, S. Liu and F. Yan, *Adv. Mater.*, 2015, **27**, 3632.

33.　C. Zhang, S. Wang, H. Zhang, Y. Feng, W. Tian, Y. Yan, J. Bian, Y. Wang, S. Jin and S. M. Zakeeruddin, *Energy Environ. Sci.*, 2019, **12**, 3585.

34.　A. Mei, X. Li, L. Liu, Z. Ku, T. Liu, Y. Rong, M. Xu, M. Hu, J. Chen and Y. Yang, *Science*, 2014, **345**, 295.

35.　F. Fu, T. Feurer, T. Jäger, E. Avancini, B. Bissig, S. Yoon, S. Buecheler and A. N. Tiwari, *Nat. Commun.*, 2015, **6**, 1.

36.　J. H. Lee, J. H. Heo, S. H. Im and O. O. Park, *ACS Appl. Mater. Interfaces*, 2020, **12**, 10527.

37.　J. P. Singh, T. M. Walsh and A. G. Aberle, *Progress in Photovoltaics: Research and Applications*, 2014, **22**, 903.

38.　N. Boukortt and B. Hadri, *Indian J. Phys.*, 2019, **93**, 33.
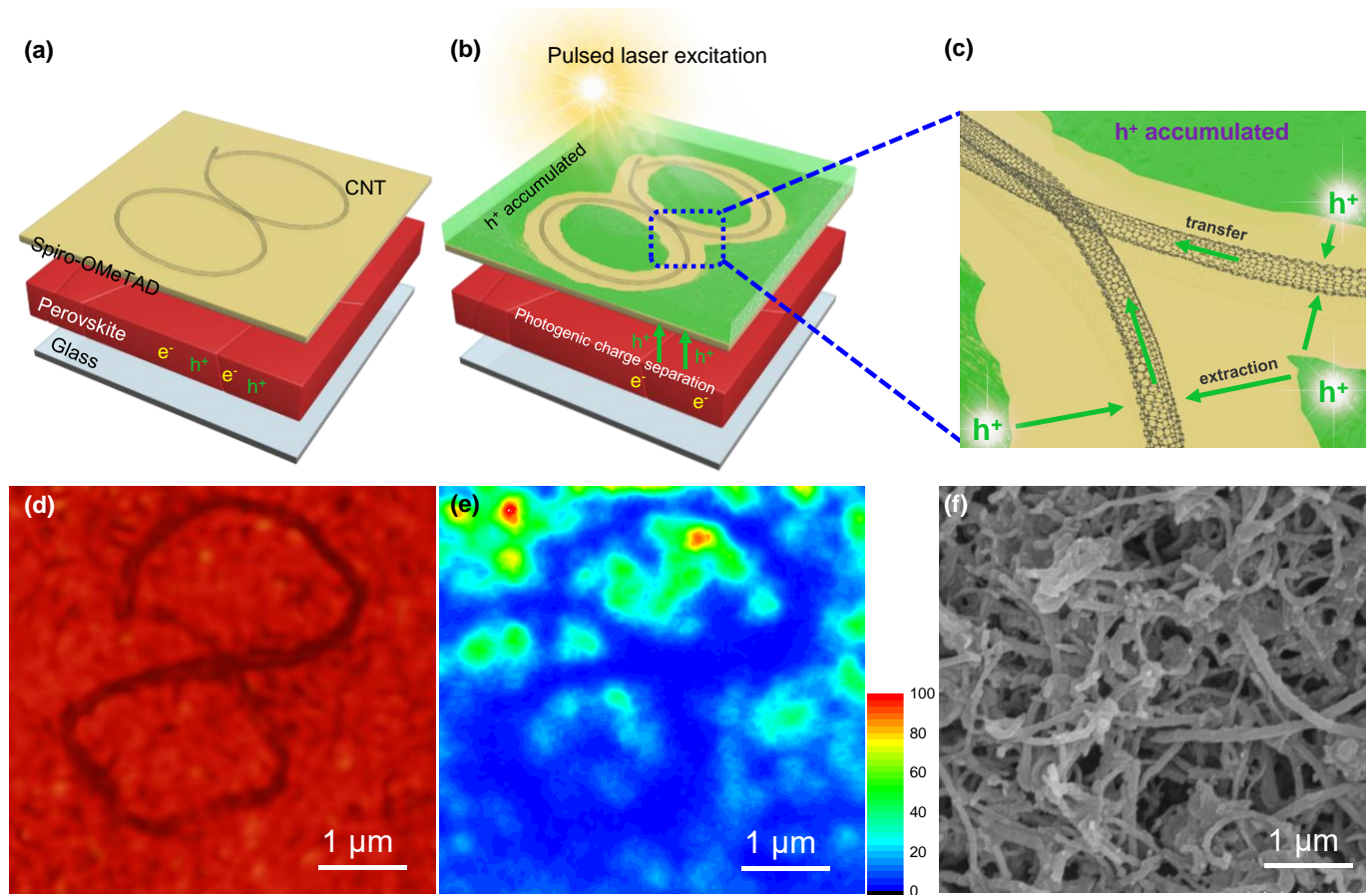
ARTICLE

Fig. 1 (a) Schematic of the device structure glass/perovskite/spiro-OMeTAD. (b) The schematic diagram of light excitation fluorescence for structure in a. (c) Enlarger diagram of schematic diagram in b. (d and e) Optical image (d) and PL map of intensity (e) based on the perovskite/(MWCNT/1). The red part of optical image is perovskite and the black part is MWCNT/1. The white circles indicate the outline of carbon material. The color bar indicates the fluorescence intensity emitted from the sample. (f) The SEM image of MWCNT/1 film sprayed on glass.
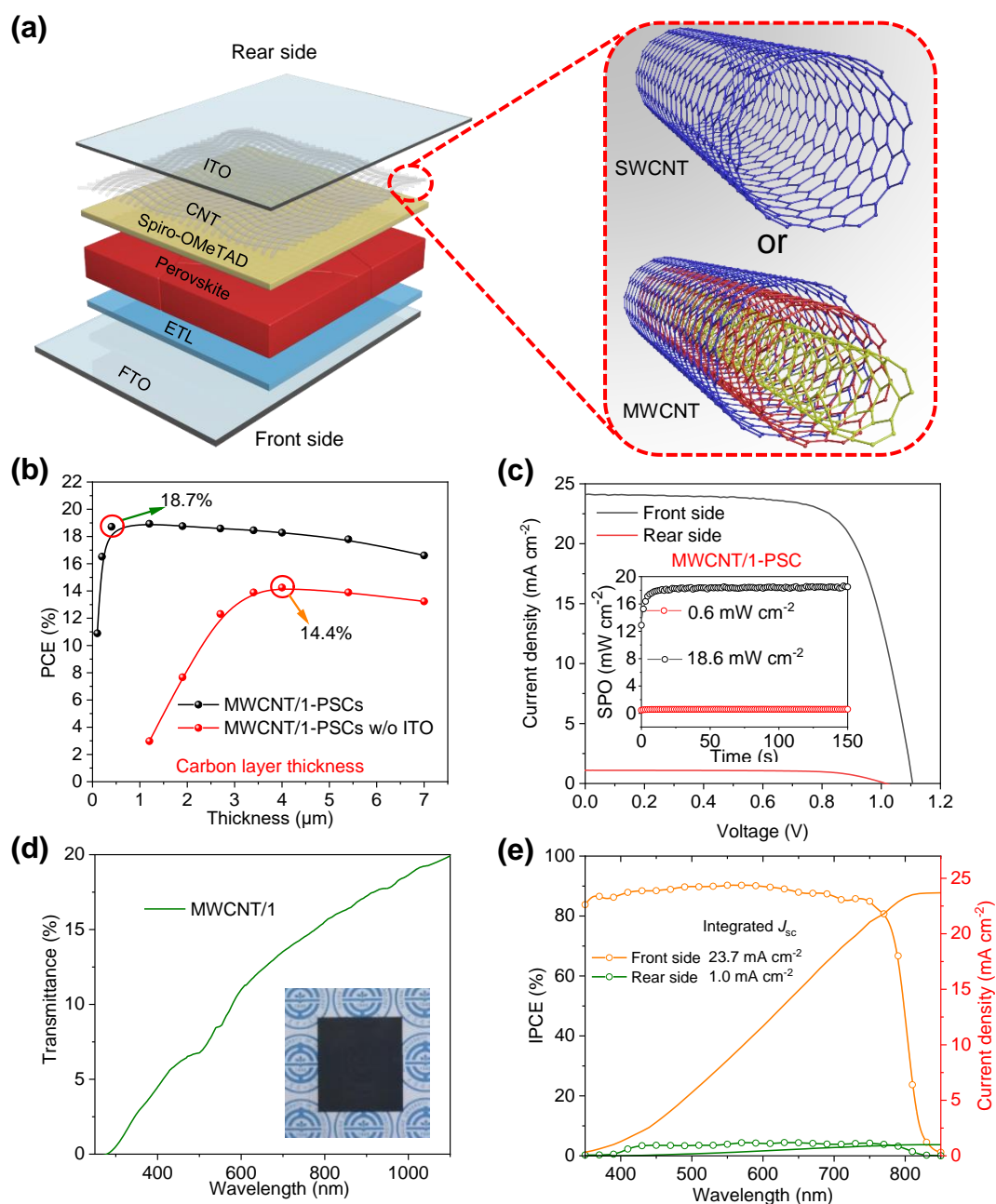
Fig. 2 (a) Schematic illustration of bifacial CNT-PSC. (b) Trend curve of PCE changes with increasing the carbon layer thickness for MWCNT/1-PSC and MWCNT/1-PSC as reference. (c) The *J-V* curves and steady state power output curves (inset) of MWCNT/1-based bifacial solar cell illuminated from front side and rear side, respectively. (d) UV-Vis transmission spectrum and optical image of MWCNT/1 film sprayed on glass. (e) EQE of MWCNT/1-based bifacial solar cell illuminated from front side and rear side, respectively.
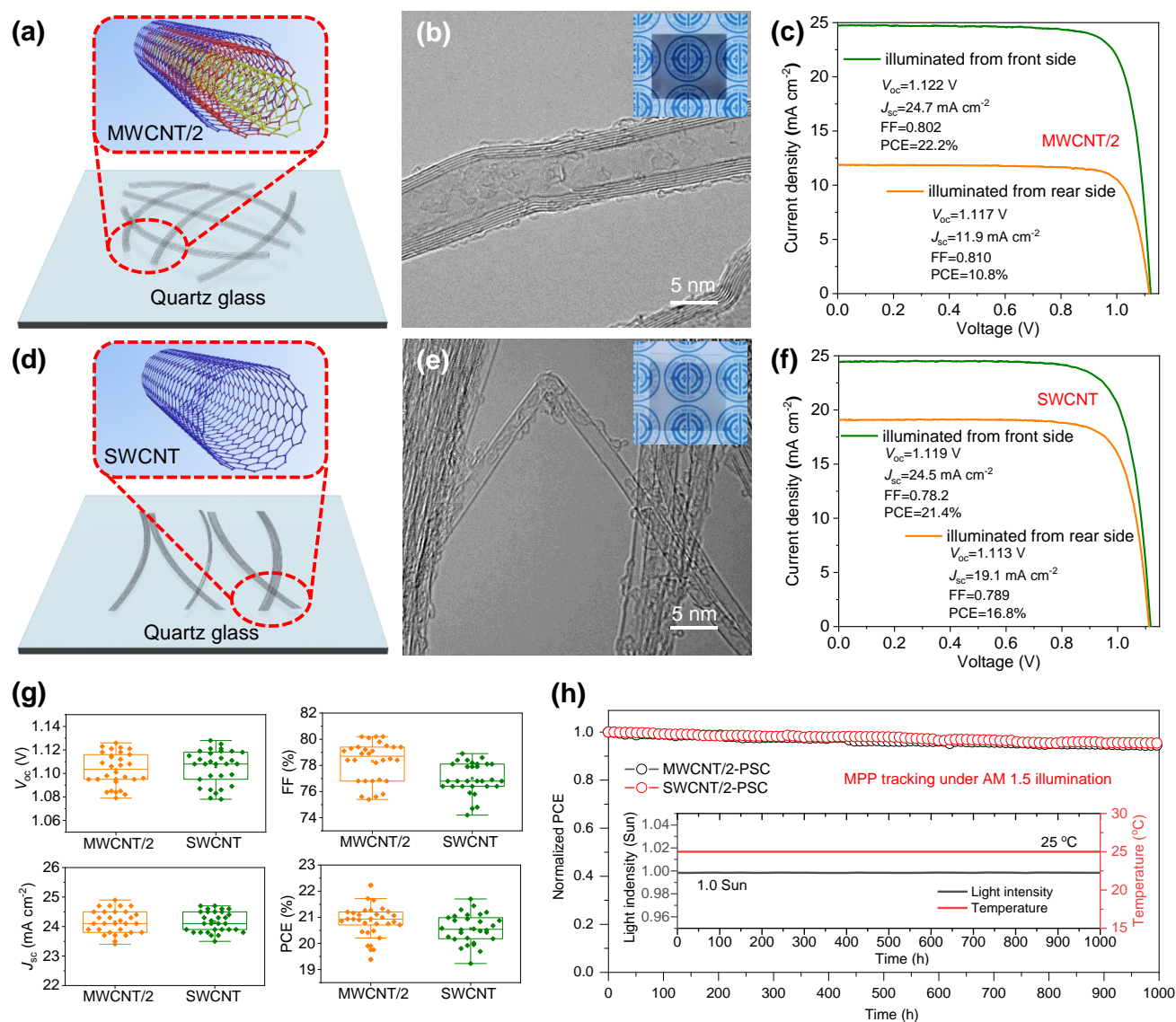
Fig. 3 (a and b) The diagram (a) and TEM image (b) of MWCNT/2 film (thickness: 100 nm) sprayed on glass. (c) The *J-V* curves of MWCNT/2-based bifacial solar cell illuminated from front side and rear side, respectively. (d and e) The diagram (d), SEM image (e) of SWCNT film (thickness: 100 nm) sprayed on glass. (f) The *J-V* curves of MWCNT/2-based bifacial solar cell illuminated from front side and rear side, respectively. (g) PV Performance parameter statistics of bifacial CNT-PSC illuminated from front side based on MWCNT/2 and SWCNT electrode. (h) Maximum power point (MPP) ageing of MWCNT/2-PSC and SWCNT-PSC under N_2 atmosphere, 1 sun continuous illumination (25 $^{\circ}$C).

Table 1 Photovoice performance parameters of MWCNT/2-PSCs and SWCNT-PSCs illuminated from front side and rear side separately.

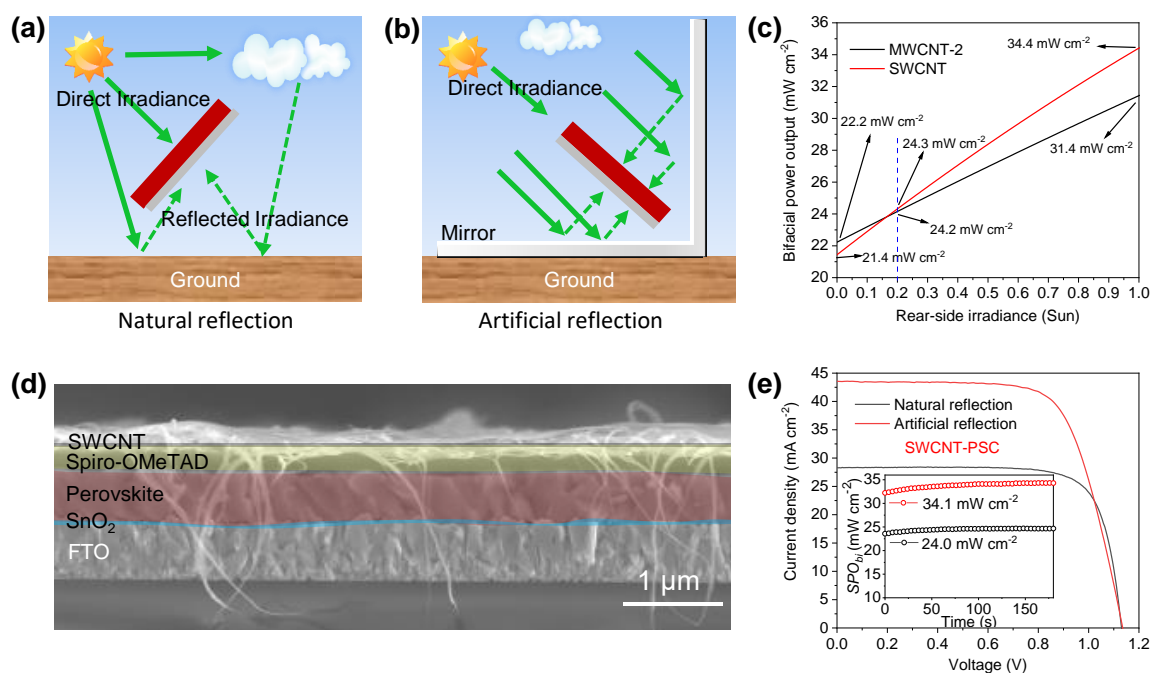|		V_{oc} [V]	J_{sc} [mA cm^{-2}]	FF [%]	PCE [%]	Illuminate from
MWCNT/2	Average	1.103±0.014	24.2±0.4	78.3±1.5	20.9±0.6	Front side
	Champion	1.122	24.7	80.2	22.2	Front side
	Champion	1.117	11.9	81.0	10.8	Rear side
SWCNT	Average	1.105±0.014	24.2±0.3	77.0±1.2	20.6±0.6	Front side
	Champion	1.119	24.5	78.2	21.4	Front side
	Champion	1.113	19.1	78.9	16.8	Rear side

Fig. 4 (a and b) Schematic diagram of bifacial solar cell making full use of sunlight from front and rear side irradiances. (c) Theoretical PO_{bi} trend curves of bifacial MWCNT/2-PSC and SWCNT-PSC under 1 sun front side irradiance and different rear side irradiance. (d) Cross-section SEM image of semi-cell A in SWCNT-PSC. (e) The *J-V* curves and steady-state bifacial power output (SPO_{bi}) curves (inset) of SWCNT/1-PSC under natural reflection and artificial reflection, respectively.
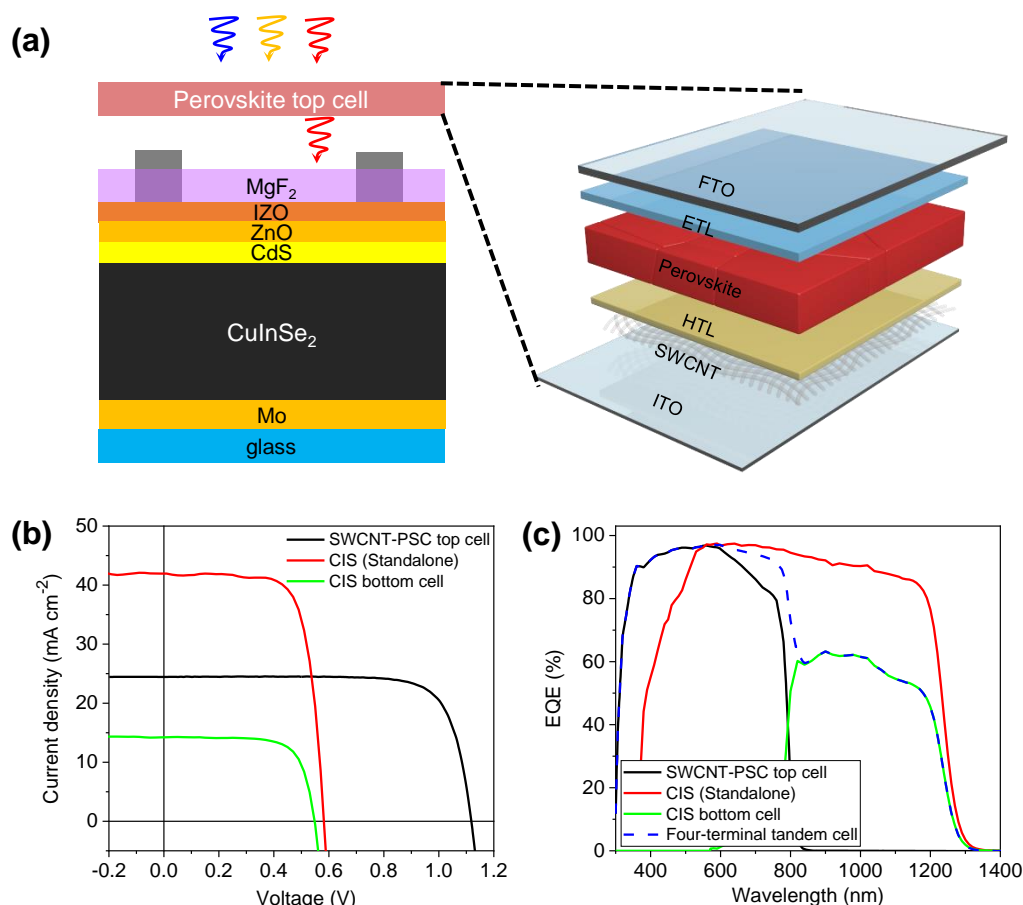
Fig. 5 (a) Structural diagram of SWCNT-PSC/CIS 4-T tandem solar cell. (b and c) The *J-V* curves (b) and EQE spectra (c) of the 4-T tandem device. The EQE curve of SWCNT-PSC/CIS 4-T tandem solar cell is obtained by adding the EQE curve of the SWCNT-PSC top cell and the CIS bottom cell.

Table 2 The PV parameters of the SWCNT-PSC/CIS 4-T tandem solar cell.

Solar cell	V_{oc} [V]	J_{sc} [mA cm^{-2}]	Calculated J_{sc} [mA cm^{-2}]	FF [%]	PCE [%]	PCE with SPO [%]
SWCNT-PSC top cell	1.119	24.5	24.0	78.2	21.4	21.4
CIS standalone	0.584	42.0	42.7	73.1	17.9	17.9
CIS bottom cell	0.549	14.3	13.7	72.4	5.7	5.7
SWCNT-PSC/CIS 4-T tandem cell						27.1